Disruption of Circadian Clock Induces Abnormal Mammary Morphology and Aggressive Basal Tumorigenesis by Enhancing LILRB4 Signaling

Short title: Circadian disruption causes tumorigenesis via LILRB4

Authors

Olajumoke Ogunlusi,[1†] Mrinmoy Sarkar,[1†] Arhit Chakrabarti,[2] Devon J Boland,[3] Tristan Nguyen,[1] James Sampson[4], Christian Nguyen,[1] Danielle Fails,[5] Yava Jones-Hall,[6] Loning Fu,[7] Bani Mallick,[2] Alex Keene,[1] Jeff Jones,[1] Tapasree Roy Sarkar[*1]

Affiliations

[1]Department of Biology, Texas A&M University, College Station, TX, USA.

[2]Department of Statistics, Texas A&M University, College Station, TX, USA.

[3]Texas A&M Institute of Genome Sciences & Society (TIGSS), College Station, TX, USA.

[4] Department of Biomedical Engineering, Texas A&M University, College Station, TX, USA.

[5]Fortis Life Sciences, Montgomery, TX 77356, USA.

[6]Veterinary Pathobiology, Texas A&M University, College Station, TX, USA.

[7]Baylor College of Medicine, Houston, TX, USA.

[*]**Corresponding author:** tsarkar@bio.tamu.edu.

[†] These authors contributed equally to this work.

Abstract

Epidemiological studies have shown that circadian rhythm disruption (CRD) is associated with the risk of breast cancer. However, the role of CRD in mammary gland morphology and aggressive basal mammary tumorigenesis and the molecular mechanisms underlying CRD and cancer risk remain unknown. To investigate the effect of CRD on aggressive tumorigenesis, a genetically engineered mouse model that recapitulates the human basal type of breast cancer was used for this study. The effect of CRD on mammary gland morphology was investigated using wild-type mice model. The impact of CRD on the tumor microenvironment was investigated using the tumors from LD12:12 and CRD mice via scRNA seq. ScRNA seq was substantiated by multiplexing immunostaining, flow cytometry, and realtime PCR. The effect of LILRB4 immunotherapy on CRD-induced tumorigenesis was also investigated. Here we identified the impact of CRD on basal tumorigenesis and mammary gland morphology and identified the role of LILRB4 on CRD-induced lung metastasis. We found that chronic CRD disrupted mouse mammary gland morphology and increased tumor burden, and lung metastasis and induced an immunosuppressive tumor microenvironment by enhancing LILRB4a expression. Moreover, CRD increased the M2-macrophage and regulatory T-cell populations but decreased the M1-macrophage, and dendritic cell populations. Furthermore, targeted immunotherapy against LILRB4 reduced CRD-induced immunosuppressive microenvironment and lung metastasis. These findings identify and implicate LILRB4a as a link between CRD and aggressive mammary tumorigenesis. This study also establishes the potential role of the targeted LILRB4a immunotherapy as an inhibitor of CRD-induced lung metastasis.

Keywords

Circadian rhythm disruption, breast cancer, LILRB4, tumor microenvironment, immunotherapy.

Introduction

The circadian clock regulates the expression of several genes that impact physiology, metabolic processes, and health outcomes (Panda, Antoch et al. 2002, Storch, Lipan et al. 2002, Kelleher, Rao et al. 2014). Epidemiological studies have reported that circadian rhythm disruption (CRD), such as that which occurs during shift work or travel across time zones, affects human health and increases the risk of developing cancer, metabolic disorders, and cardiovascular disease (Hemmer, Mareschal et al. 2021). According to the National Health Interview Survey, 12–35% of the US population works irregular schedules, including night and rotating shifts (CDC 2015). CRD increases the risk of different types of cancer, including lung (Papagiannakopoulos, Bauer et al. 2016, Pariollaud, Ibrahim et al. 2022), colon (Chun, Fortin et al. 2022), and breast (Van Dycke, Rodenburg et al. 2015, Hadadi 2020) cancers.

Shiftwork was found to increase the incidence of breast cancer in nurses by approximately 50%, suggesting a critical role for the circadian clock in breast cancer pathogenesis (Schernhammer, Laden et al. 2001). Circadian clocks regulate the rhythmic expression of numerous genes in breast tissues (Blakeman, Williams et al. 2016). Triple-negative breast cancer (TNBC) or basal phenotype (Alluri and Newman 2014) encompasses a breast tumor subtype that is clinically negative for the expression of the estrogen (ER) and progesterone (PR) receptors and lacks overexpression of the Human Epidermal Growth Factor Receptor 2 (HER2) protein, with unique prognostic and therapeutic implications (Anders and Carey 2008). TNBC is responsible for more than 15–20% of all breast cancers, with a mortality rate of 40% (Almansour 2022). TNBC is relatively aggressive and shows more resistance to chemotherapy than other subtypes of breast cancer (Almansour

80 2022). However, the effect of CRD on aggressive TNBC is poorly understood, and the precise
81 mechanism underlying CRD-induced tumorigenesis is not yet known.
82 The mammalian circadian machinery consists of an autoregulatory transcription-translation
83 feedback loop, where the "positive elements" circadian locomotor output cycle kaput (CLOCK)
84 and brain and muscle aryl hydrocarbon receptor nuclear translocator (ARNT)-like protein 1
85 (BMAL1) heterodimerize through their PAS domains and activate the transcription of the
86 "negative elements," i.e., the period genes (*Per1* and *Per2)* and the cryptochrome genes (*Cry1* and
87 *Cry2)*. The PER/CRY heterodimers inhibit the transcription of their gene(s) by blocking
88 CLOCK/BMAL1-dependent transactivation (Kelleher, Rao et al. 2014). This feedback loop
89 regulates the transcription of an estimated 30% of the genome (Vitaterna, Shimomura et al. 2019).
90 The expression of core circadian clock genes is frequently dysregulated in human tumors,
91 indicating the tumor-suppressive role of the molecular clock (Battaglin, Chan et al. 2021,
92 Stephenson, Usselmann et al. 2021, Chun, Fortin et al. 2022). Epidemiological studies have also
93 emphasized that the risk of developing cancer increases with increasing years of shift work (Yuan,
94 Zhu et al. 2018), indicating that longitudinal experiments are better suited for characterizing how
95 CRD may affect tumorigenesis.
96 Here, we investigated how the loss of circadian function impacts mammary glands, tumorigenesis,
97 and the tumor microenvironment (TME). We used the jet lag schedule, which mimics the circadian
98 disturbance humans encounter during rotating shift work or frequent jet lag, and the genetically
99 engineered mouse model (GEMM) of TNBC. We specifically examined the role of leukocyte
100 immunoglobulin-like receptor 4a (LILRB4a or LILRB4 or gp49B), which is known to suppress
101 immunity in acute myeloid leukemia (AML) and solid tumors (Deng, Gui et al. 2018, Sharma
102 2021). Additionally, we investigated whether the elevation of LILRB4 expression could be a key

molecular event in CRD-induced mammary tumorigenesis and immunosuppressive TME. Overall, this study shows how circadian desynchronization affects mammary gland morphology, aggressive mammary tumorigenesis, and identifies a compelling target for immunotherapy of CRD-induced tumorigenesis.

Methods

A. Animal husbandry:

The mice were housed under 12 h light and 12 h dark (LD 12:12) and circadian rhythm disruption (CRD) conditions at room temperature (25°C), and food and water were provided *ad libitum*. The genetically engineered mice model (GEMM), i.e., FVB-Tg(C3-1-Tag)cJeg/JegJ mice (Jax stock #013591), were caged until they were 27 weeks old. Normal FVB mice (Jax stock #001800) and BALB/cJ mice (Jax stock #000651) were also used in this study. All animal care and treatments were per the Institutional Animal Care and Use Committee of Texas A&M University under protocol # 2022-0094.

Mice were grouped randomly for exposure to standard light conditions (LD 12:12) or CRD light conditions (consisting of an 8-hour light phase advance repeated every two days) (Casiraghi, Oda et al. 2012, Papagiannakopoulos, Bauer et al. 2016, Pariollaud, Ibrahim et al. 2022). Zeitgeber time (ZT) 0 corresponded to the onset of light, while ZT12 corresponded to the onset of dark. The LD 12:12 and CRD animal groups were provided access to running wheels (Columbus Instruments) for several weeks. ActogramJ (ImageJ) was used to assess voluntary running activities (Schmid, Helfrich-Förster et al. 2011).

B. 4T1 cell mouse TNBC model:

125 The 4T1 cells were maintained RPMI-1640 (ATCC, 30-2001) supplemented with in 10%
126 FBS and 1% penicillin and streptomycin in 5% CO_2. Briefly, 10,000 cells suspended in
127 sterile PBS were injected subcutaneously into the 4th mammary gland fat pad. The mice
128 were housed in LD or CRD conditions for 3-4 weeks before they were sacrificed to harvest
129 the tumors. To investigate the effect of immunotherapy on tumor progression and
130 metastasis, BALB/cJ mice were housed under LD 12:12 conditions for 4-5 days following
131 injection of 4T1 cells until palpable tumors developed. They were segregated and assigned
132 randomly either in LD or CRD conditions. On days 6, 9, and 12 (after the palpable tumors
133 developed), an anti-LILRB4 antibody (ABclonal, #A7073) (polyclonal, 50µg) was injected
134 intratumorally. The animals were checked regularly to observe their body weight and tumor
135 sizes.

136 **C. Histology and tumor burden analysis:**

137 The tumors and the mammary glands were harvested using aseptic techniques. Tumor
138 volumes were calculated for each breast tumor using caliper measurements after every 3
139 days. $Tumor\ volume\ = (length\ \times width\text{^}2\ )/2$ was used to measure the volume of the
140 tumors (Kersemans, Cornelissen et al. 2013), whereas the equation
141 $Tumor\ burden\ (in\ percentage)\ = (Tumor\ weight\ /mice\ body\ weight) \times 100\ \%$
142 was considered to determine the tumor burden (Hadadi 2020). The tumor, or the lung
143 samples were fixed in 10% neutral buffered formalin (NBF) for 48 hours before being
144 transferred to the Histology core facility at Texas A&M University. The tissue sections
145 were stained with hematoxylin and eosin (H&E) for pathological examinations.

146 **D. Immunohistochemistry:**

147 The formalin-fixed paraffin-embedded (FFPE) mouse mammary gland tissues were
148 deparaffinized by incubating at 65°C for 2 hours, followed by dipping in xylene for 5
149 minutes each time for two changes. The endogenous peroxidase activity was inhibited by
150 treating the tissue with hydrogen peroxide. Antigen retrieval was carried out by incubating
151 the slides in pre-heated citrate antigen retrieval buffer (10 mM citrate, 0.05% Tween 20,
152 pH 6.0) at 95°C for 20-25 minutes in a water bath. After blocking, the tissues were
153 incubated overnight at 4°C with anti-ki67 polyclonal antibody (ABclonal, A16919),
154 dissolved in the kit blocking solution. Following incubation with the secondary antibody
155 availed with the IHC kit, the expression was visualized with DAB peroxidase substrate
156 (Abcam, ab64264). The slides were counterstained with Mayer's Hematoxylin Solution
157 (VitroVivo Biotech, VB-3000-1) before being mounted with Optic Mount I™ xylene
158 mounting medium (Mercedes Scientific) and imaged under the Echo Revolve R4
159 fluorescent microscope (Echo).

160 **E. Whole mount staining of mouse mammary gland:**

161 The mammary gland tissues were spread on glass slides immediately after harvesting. The
162 mammary glands were then fixed using Carnoy's fixative solution (VitroVivo Biotech, VB-
163 3001-1) for three hours, followed by washing in 70% ethanol for 30 minutes. The tissues
164 were incubated overnight at room temperature (RT) with Carmine Alum Staining Solution
165 (VitroVivo Biotech, VB-3001-2). Stained tissues were dehydrated with gradients of ethanol
166 concentrations and finally with three changes of xylene bath of 10 minutes each. The slides
167 were then mounted with Optic Mount I™ xylene mounting medium (Mercedes Scientific)
168 and observed under the microscope.

169 **F. Single-cell RNA sequencing (scRNA Seq):**

170 After brief washing in chilled sterile PBS, the tumors were kept in DMEM (ATCC, 30-
171 2002), supplemented with 10% FBS (Sigma-Aldrich, F2442) and 1% antibiotic solution
172 (Sigma Aldrich, P4333) on ice until minced and subsequently blended with gentleMACS
173 Dissociator (Miltenyi Biotec, 130-093-235). MACS Miltenyi Tumor Dissociation Kit for
174 mice (Miltenyi Biotech, 130-096-730) was used for further enzymatic digestion according
175 to the manufacturer's protocol. The suspension of cells was then transferred to the Texas
176 A&M Institute for Genome Sciences and Society (TIGSS) for scRNA-seq. Single-cell
177 sequencing libraries were prepared on the Chromium platform (10x Genomics) using the
178 Single Cell 5' v2 Full Kit (PN-1000263). Cell type assignment was performed manually
179 based on unique marker genes identified in each cell cluster from the UMAP reduction.
180 Markers were cross-referenced with published literature specific to mouse mammary gland
181 tissues. Differentially expressed genes were identified using the MAST (Finak, McDavid
182 et al. 2015) R package, and GO pathway enrichment analysis was performed with the
183 clusterProfiler (Wu, Hu et al. 2021) R package. The CellChat R package analyzed cellular
184 communication using default parameters. The most significant pathways were identified
185 using the "rankNet" function and visualized with the "netVisual_diffInteraction" function.

186 **G. *In vitro* tumorosphere formation assay:**

187 The single cells (from tumors) were cultured in ultra-low attachment 96-well plates
188 (ThermoFisher Scientific, 174927) in EpiCult™-B (mouse) medium supplemented with
189 human recombinant EGF (hrEGF) (Stem Cell Technologies, 78006), human recombinant
190 bFGF (hrbFGF) (Stem Cell Technologies, 78003), and heparin (Stem Cell Technologies,
191 07980). 500 cells per well from LD 12:12 and CRD group tumors were added and

192 incubated with standard cell culture conditions for 5 days in the CO_2 incubator before being
193 observed under the microscope.

194 H. **Organoid assay:**

195 Singlet cells from tumors (LD and CRD) were resuspended in Geltrex™ (Gibco,
196 ThermoFisher, A1413202) and plated on a 24-well plate. After the gel was solidified to
197 form the matrix, EpiCult™-B (mouse) medium supplemented with hrEGF, hrbFGF, and
198 heparin was added to assess the growth of the mouse mammary tumor cells from LD 12:12
199 and CRD conditions. After 7 days of incubation, the organoids formed were imaged under
200 the microscope.

201 **I. Flow cytometry:**

202 The dissociated tumor cells were counted and resuspended in 1 ml of cell staining buffer
203 (CSB) (BioLegend, 420201). Zombie NIR™ Fixable Viability Kit (BioLegend, 423105)
204 was applied to cells on ice for 20 min. After spinning down at 400 x g for 4 minutes, cells
205 were resuspended in 50 µl of the CSB and incubated with fluorochrome-conjugated
206 antibodies (Alexa Fluor® 700 anti-mouse CD4, Pacific Blue™ anti-mouse CD8a, Alexa
207 Fluor® 488 anti-mouse CD86, PE anti-mouse CD163, Alexa Fluor® 594 anti-mouse
208 CD45, FITC anti-mouse Ly-6G/Ly-6C, PE anti-mouse/human CD11b, Alexa Fluor® 647
209 anti-mouse I-A/I-E, FITC anti-mouse CD11c) in the dark for 20 minutes, following a
210 systematic approach via designing compatible multicolor flow cytometry panels. Cells
211 were fixed and permeabilized using 2% paraformaldehyde and 0.1% Triton X-100 in PBS,
212 respectively, and stained with anti-FoxP3 antibody (Alexa Fluor® 488 anti-
213 mouse/rat/human FOXP3) for 20 minutes in the dark at 4°C, in case of tumor infiltrated
214 lymphocyte-specific panel. Afterward, stained cells were rinsed with PBS and kept in PBS

215 at 4°C in the dark until analyzed using Cytek Aurora spectral flow cytometer at TAMU
216 Flow Cytometry Facility.

217 **J. Quantitative PCR for detecting mRNA levels:**

218 Total RNA was extracted from mammary glands or tumors using Quick-RNA™ MiniPrep
219 (Zymo Research, R1054), and the purity was analyzed by DeNovix DS-11 Series nanodrop
220 Spectrophotometer (DeNovix). RNA from each sample was reverse transcribed to cDNA
221 by High-Capacity cDNA Reverse Transcription Kit (Applied Biosystems™, 4368814).
222 Analysis for gene expression by quantitative real-time PCR was performed using
223 SsoAdvanced Universal SYBR Green Supermix (BioRad, 1725271).

224 **K. Human CRD analysis for breast cancer patients:**

225 All statistical analyses were performed using the R software package (version 4.3.0.).
226 scRNA-seq data corresponding to the triple-negative breast cancer (TNBC) patients from
227 Wu *et al.*, 2021 (Wu, Al-Eryani et al. 2021) were pre-processed using standard steps
228 outlined in Hao *et al.,* (Hao, Hao et al. 2021). The uniform manifold approximation and
229 projection (UMAP) was performed on the processed data. The UMAP plot with cells
230 clustered according to the inferCNV cell type. The cells which had no infer-CNV call are
231 denoted as "unknown." To investigate the level of circadian rhythm disruption in each cell,
232 we calculated the CRD scores for the 358 circadian-related genes (CRGs) following He *et*
233 *al.,* 2022 (He, Fan et al. 2022) separately for malignant and non-malignant cells. A cutoff
234 of 75% based on quartiles was used as the threshold for the CRD level to segregate the
235 scores as high (denoted as CRD^{hi}) and low (denoted as CRD^{low}). The percentage of cells
236 that show CRD^{hi} scores by cell type, along with the p-value of the corresponding Binomial
237 proportion test, is used for this study. The mean normalized expression of the core

238 circadian genes by the cell type (malignant and non-malignant) is presented in this study.
239 Bulk RNA-sequencing data from the publicly available TCGA BRCA dataset was used
240 further to explore the expression pattern of the core circadian genes. The patients were
241 segregated according to the analyzed tissue type, i.e., "Tumor" and "Surrounding" tissue.
242 The mean expression of the genes (+/- SEM) over patients by the type of tissue analyzed.
243 The Wilcoxon signed-rank test was used to test for the difference in expression between
244 the tumor and surrounding tissues for each gene. The genes showing a significant
245 difference are labeled in "red", while the insignificant genes are marked in "black".

246 **L. Blood chemistry and cytokine array:**

247 Pre-mortem terminal blood was collected from the FVB-Tg(C3-1-Tag)cJeg/JegJ mice. The
248 blood samples were transferred to the Texas A&M TVMDL to analyze the blood chemistry
249 parameters. The cytokine array was performed using the Proteome Profiler Mouse XL
250 Cytokine Array kit (R&D Systems, ARY028). The blood samples were kept undisturbed
251 for 30 minutes at room temperature before being spun at 2000 x g for 10 minutes at 4°C.
252 The serum was separated for the cytokine array profiling according to the manufacturer's
253 protocol and was scanned using ChemiDoc Imaging System (BioRad, 12003153).

254 **M. mIF Staining of Mouse Tissues:** The panels were developed and optimized for use in
255 mouse tissue. The following primary antibodies from Fortis Life Sciences, Cell Signaling
256 Technology, and ABclonal were utilized for both immunohistochemical and
257 immunofluorescence staining: rabbit anti-mouse ARG1 [BLR161J], rabbit anti-
258 human/mouse LILRB4 [A7073], rabbit anti-human/mouse CD163 [BLR087G], rabbit
259 anti-mouse CD8a [BLR173J], and rabbit anti-mouse FOXP3 [D6O8R], and rabbit anti-
260 mouse CD4 [BLR167J]. Multiplex immunofluorescence staining was performed with the

261 Akoya Opal™ Polaris 7-color IHC kit fluorophores (Akoya Biosciences
262 [NEL861001KT]). FFPE tissue sections were baked for 30 minutes, deparaffinized in
263 xylene, and rehydrated by serial passage through graded concentrations of ethanol.
264 Endogenous peroxidase in tissues was blocked with 0.9% H_2O_2/methanol for 40 min.
265 Multiple (7) sequential HIER treatments were performed for 20 min each at 92-96°C in
266 Citrate pH 6.0 (first cycle) or Tris EDTA pH9 (remaining cycles) buffer. After each HIER
267 cycle, sections were rinsed with DI water and cooled at RT for 20 minutes. Tissue sections
268 were blocked with 20% normal goat serum for 20 minutes before incubation with primary
269 antibody for 20 min. Then, sections were rinsed with TBST for 10 min and incubated with
270 HRP-conjugated secondary (A120-501P) for 20 min, followed by another 10 min rinse in
271 TBST. Incubation with an Opal fluorophore (Opal480, Opal520, Opal570, Opal620,
272 Opal690) was then done for 10 min, followed by a 10 min rinse in DI water. Bound primary
273 and secondary antibodies were then subject to the next HIER treatment (as aforementioned)
274 for 20 min. After washing in DI water and cooling at RT for 20 min, the process of staining
275 and antibody removal was repeated for the desired number of targets. Finally, the tissue
276 specimens were stained with 4′,6-diamidino-2-phenylindole (DAPI) for 10 min and
277 mounted in VECTASHIELD Vibrance Antifade Mounting Medium (ThermoFisher
278 Scientific). Akoya Biosciences' PhenoImager HT was used for multispectral imaging at
279 40× magnification.
280

281 **N. Statistical analysis:**

282 GraphPad Prism8 was used as the Statistical analysis tool except for the assessment of the
283 rhythmicity that was carried out using the JTK cycle. The significance was assessed using

284 either an Unpaired t-test or analysis of variance (ANOVA), with a false positive threshold
285 of 0.05 considered acceptable ($p<0.05$). Unless otherwise mentioned, the data were
286 presented as mean ± standard error of mean (SEM).
287

288 **Results**

289 **Chronic CRD results in abnormal mammary gland morphology**

290 The jet-lag paradigm mimics the CRD that humans face during shift work (Lee, Donehower et al.
291 2010) or travels across time zones. Mice were exposed to an 8 h light advance repeated every 2–3
292 days (Fig. 1A). Female Friend LeukemiaVirus B (FVB) mice (4 weeks old) were housed under
293 normal light and dark (LD 12:12), or chronic CRD conditions for 8 weeks before the mammary
294 glands were collected every 4 h for 24 h. We confirmed that this jet-lag protocol disrupted
295 circadian activity in our mouse model by assessing the locomotor activity (Fig. 1B). CRD did not
296 significantly impact the weight of mice (Fig. S1A). Real-time PCR analysis showed that CRD led
297 to the loss of rhythmicity (*P*JTKcycle < 0.05) for most genes, including *Cry1*, *Cry2*, *Bmal1*, *Clock,*
298 and *Per1* (Fig. 1C). *Per2* expression remained rhythmic in mice exposed to CRD (Fig. 1C),
299 suggesting the desynchronization of the core clock components. To understand the effect of CRD
300 on the mammary glands, we examined whole-mount preparations of inguinal mammary glands
301 from LD and CRD mice at 12 weeks. Chronic CRD decreased branching (bifurcations) (Fig. 1D,
302 upper panel, 1E, S1B) and the number of terminal end buds (TEBs) (Fig. 1D, lower panel, 1F,
303 S1B) in the mammary glands. Compared with the mammary glands of LD mice (control), CRD
304 mice showed a high frequency of ductal hyperplasia as found by using hematoxylin and eosin
305 (H&E) (Fig. 1G) and by using Ki67 (Fig. 1H, S1C) staining of the mammary glands.

306 **Chronic CRD accelerates aggressive mammary tumorigenesis and lung metastasis**

307 To investigate the effect of CRD on aggressive basal tumorigenesis, we used preclinical GEMM
308 of human basal tumors (FVB-Tg(C3-1-Tag)cJeg/JegJ (Maroulakou, Anver et al. 1994, Usary
309 2017) that provides a model for examining how CRD impacts aggressive mammary tumorigenesis
310 and metastasis. Female hemizygous mice develop mammary gland adenocarcinomas at
311 approximately 24 weeks of age (Maroulakou, Anver et al. 1994, Usary 2017). To investigate the
312 effect of CRD on tumorigenesis, mice were placed under LD or CRD conditions when they were
313 8 weeks old and maintained under CRD conditions through the end of the study at 27 weeks (Fig.
314 2A). The growth of primary tumors was measured every 3 days throughout this period. Because
315 of the highly aggressive tumors in CRD mice, we euthanized the animals at 27 weeks. All mice
316 were euthanized, and the tumor tissues were processed for other analyses. CRD did not
317 significantly impact the weight of mice (Fig. S2A). Peripheral blood cell counts showed no
318 significant differences between those mice (Fig. S2B, S2C). No significant changes were noted in
319 the blood glucose, cholesterol, or amylase (Fig. S2D-F) levels in CRD mice, although the albumin-
320 to-globulin ratio (AGR) was decreased (Fig. S2G). A high AGR shows a good prognosis for
321 survival in different solid-tumor patients (He, Pan et al. 2017). Therefore, CRD negatively affects
322 cancer prognosis by decreasing the AGR. scRNAseq (Fig. S3A) and real-time PCR (Fig. S3B) of
323 tumor samples showed that CRD did not substantially alter the expression of Per genes (*Per1*, and
324 *Per2*) (Fig. S3A, B) or other clock genes (*Clock*, *Cry2*) (Fig. S3A, B). *Cry1* expression
325 significantly increased in CRD-induced tumors (Fig. S3B).
326 Animals placed in CRD conditions had a substantially increased mammary tumor burden (Fig. 2B)
327 compared to the LD animals. CRD also accelerated tumor initiation at 18 weeks. In contrast, the
328 average time of tumor initiation for LD mice was 22 weeks (Fig. 2C). However, no difference was
329 observed in the spectrum of tumor grades assessed using histopathology (Elston and Ellis 2002)

330 between the two groups, with most tumors being grade 2 (Fig. S4A, B). Several technical
331 differences, such as in the mouse genetic background (MMTV:PyMT C57BL/6J versus FVB-
332 Tg(C3-1-TAg)cJeg/JegJ) and conditions of the animal facilities (such as light exposure) may
333 explain why Hadadi *et al.* (Hadadi 2020) observed an effect of CRD on tumor grade, but the same
334 was not found in our study. The number of metastatic foci in the lungs was significantly higher in
335 the CRD mice (Fig. 2D, E). To investigate the impact of CRD on tumor progression, 4T1 (mice
336 triple-negative breast cancer cell line) cells were introduced into the female BALB/cJ mice via
337 orthotopic transplantation into the 4th mammary glands. When mice developed palpable tumors
338 (~4-5 days after injection), they were placed into LD or CRD conditions for 3 weeks until tumors
339 became aggressive. CRD led to a modest but non-significant increase in tumor burden (Fig. S4C).
340 This data suggests that CRD does not affect mammary tumor progression. However, we did
341 observe a significant increase in the formation of lung metastasis foci (Fig 2F, G). Flow cytometry
342 was performed to investigate whether a higher metastatic potential was related to a higher cancer
343 stem cell (CSC) population in CRD tumors. We observed a significant increase in the percentage
344 of CSCs expressing CD49f markers (Fig. 2H, S4D) in CRD tumors compared with that in LD
345 tumors. To investigate whether this enrichment was associated with an increase in the stemness
346 potential of primary tumors, a mammosphere assay was performed using CRD and LD GEMM
347 tumors. CRD tumor cells had a significantly higher ($P<0.0001$) mammosphere formation
348 efficiency than LD tumor cells (Fig. 2I, S4E). Recent studies have used three-dimensional (3D)
349 organoids as *in vitro* organs, with numerous applications ranging from disease modeling to drug
350 screening (Meyer, Howden et al. 2011). Using small intestinal crypt-derived organoids, a recent
351 study showed that genetic disruption of the circadian clock accelerates intestinal organoid

352 proliferation (Chun, Fortin et al. 2022). We established 3D organoids (tumoroids) from LD and
353 CRD tumors (Fig. 2J). Overall, CRD tumors exhibited more aggressive organoids than LD tumors.

354 **Circadian desynchronization alters the TME**

355 Breast TME is essential for the survival and immunosuppression of tumor cells (Binnewies,
356 Roberts et al. 2018). We performed scRNA analysis on cells isolated from GEMM basal tumor
357 tissues. Single cells were isolated from the tumors (Rodriguez de la Fuente, Law et al. 2021)
358 without surface marker selection. Using proper QC and filtration, we obtained single-cell
359 transcriptomic data for the studied tumors (N= 2/set). To analyze different cell populations in the
360 TME, 5,804 QC-positive single cells (LD and CRD tumors) were clustered according to their
361 expression profiles (Fig. 3A), and 20,764 genes were identified. The Seurat package was used for
362 preliminary clustering. Cells were clustered based on specific cell markers. Using the established
363 expression markers, such as for endothelial cells (*KLF2*)(Sangwung, Zhou et al. 2017), M2
364 macrophages (*SLC2A1*)(Wang, Wang et al. 2023), TNBC cancer cells (*TRPS1*)(Ai, Yao et al.
365 2021), proliferating cells (*TOP2A)*(Neubauer, Wirtz et al. 2016), myeloid cells (*FTH1*)(Moreira,
366 Silva et al. 2022), progenitor cells (*NES*)(Bernal and Arranz 2018), adipocytes
367 (*CLEC11A*)(Merrick, Sakers et al. 2019), mesenchymal cells (*S100A4*)(Fei, Qu et al. 2017),
368 angiogenic cells (*RPL35A*)(Wu, Al-Eryani et al. 2021), breast cancer stem cells *(FXYD3*)(Li,
369 Nishimura et al. 2023), dendritic cells or DCs (*CD68*) (Strobl, Scheinecker et al. 1998), cancer-
370 associated fibroblast or CAFs (*COL1A2*)(Han, Liu et al. 2020), epithelial cells (*EPCAM*)(Trzpis,
371 McLaughlin et al. 2007), cycling cells (*CDK4*)(Baker, Poulikakos et al. 2022), and B-cells (*CD83*)
372 (Grosche, Knippertz et al. 2020), we found that CRD altered different cell populations in the TME
373 (Fig. 3B). This showed that CRD induced a higher number of M2-macrophage, TNBC cancer cells,
374 cycling cells, adipocytes, CAFs and proliferating cells but a lower number of B-cells, and DCs in

375 the tumor (Fig. 3B). We next analyzed putative ligand–receptor (L-R) interactions in LD and CRD
376 tumors and modeled cell–cell interactions between different cell types that play vital roles in
377 maintaining cellular homeostasis. Cellular communication was investigated using CellChat, which
378 shows the differences in the total number of L-R interactions between different cell types in the
379 tumors (Fig. 3C). For example, the interaction between CAF with proliferating cells, TNBC cells,
380 and M2 macrophages increased under CRD conditions compared to LD conditions (Fig. 3C). We
381 identified 3429 and 3992 critical ligand–receptor pairings in LD and CRD tumors, respectively
382 (Fig. S5A). Ligand–receptor interactions with increased and decreased strength were also
383 identified (Fig. S5B). CellChat also identified signaling pathways linked to ligand–receptor
384 interactions (Fig. 3D). Specific signaling pathways, including those involving fibroblast growth
385 factor (FGF), WNT, and platelet-derived growth factor (PDGF), were exclusively detected in CRD
386 tumors. Oncostatin M, Tumor necrosis factor (TNF), and NOTCH, were detected solely in LD
387 tumors, and signaling pathways, including transforming growth factor β (TGFβ), epidermal
388 growth factor (EGF) and fibronectin 1, were detected in both LD and CRD tumors (Fig. 3D). Gene
389 Ontology (GO) analysis (Fig. 3E) indicated that genes associated with the acetyl CoA metabolic
390 process, antigen processing (and presentation), nuclear division, regulation of cellular pH,
391 carboxylic acid catabolic process, chromosome segregation were upregulated in CRD.
392

393 **CRD induces immunosuppressive TME and turns tumors "cold"**

394 The TME is critical for tumor progression and metastasis. Tumors are "hot" when they show signs
395 of inflammation characterized by an infiltration of T cells mobilizing to fight the cancerous cells,
396 whereas nonimmunogenic "cold" tumors lack infiltrating T cells, which makes it challenging to
397 provoke an immune response with immunotherapy drugs (Ren, Guo et al. 2022). To investigate

398 whether the increased prevalence of metastasis in CRD mice resulted from changes in the TME,
399 we characterized different immune cell populations in the TME of LD and CRD tumors using
400 scRNA-seq, flow cytometry, and immunostaining (MxIF). We determined whether CRD could
401 influence the proportion of various immune cells in the TME and, in turn, promote tumor
402 progression and metastasis. scRNA-seq with GEMM tumors showed that CRD reduced cytotoxic
403 T-cell infiltration (Fig. S6A) and enhanced regulatory T-cell (T_{reg}) infiltration (Fig. S6B). CRD-
404 induced M2-macrophage populations while decreasing M1-macrophage populations (Fig. S6C).
405 Flow cytometry analysis with CRD-induced 4T1 tumors supported the scRNA seq data. Our study
406 showed a significant inhibition of the number of infiltrating $CD8^{+}$ T cells (cytotoxic T-cells) (Fig.
407 4A) and an increase in the CD4/CD8 ratio (Fig. 4B) in CRD-induced tumors. The increased
408 CD4/CD8 ratio in CRD-induced tumors also indicates an immunosuppressive microenvironment.
409 FACS showed significant enrichment of the immunosuppressive T_{reg} ($CD4^{+}FoxP3^{+}$) population
410 (Fig. 4C) in the CRD-induced tumors. We identified anti-tumor (M1) and pro-tumor (M2)
411 macrophage populations in the LD and CRD-induced tumors. CRD induced M2-macrophage
412 infiltration while reducing M1-macrophage infiltration (Fig. 4D). Tumors from mice under CRD
413 conditions exhibited a ratio (M1:M2) that favored M2-mediated immunosuppression (Fig. 4E) and
414 facilitated tumor growth. CRD significantly enhanced the $CD45^{+}$ immune cell population in
415 tumors (Fig. 4F). CRD-induced tumors showed a lower dendritic cell population compared to LD-
416 induced tumors which support the anti-cancer properties of dendritic cells (CD11c) (Fig. 4G). Flow
417 cytometry study also showed a significant increase in the MDSC population (CD11b) (Fig. 4H) in
418 CRD-induced tumors, which further supports an immunosuppressive microenvironment. A donut
419 chart shows the differences in different immune cell populations in LD vs CRD-induced tumors
420 (Fig. 4I). Our immunofluorescence assay showed that CD8+ T-cell infiltration was decreased, but

421 M2 macrophages (CD163) and FOXP3 (T_{reg}) expression was enhanced in CRD-induced GEMM
422 tumors compared with those in LD GEMM tumors (Fig. 4J), making the tumor "cold." CRD
423 increased EMT gene expressions, such as fibronectin 1 (FN1) and Snail (SNAIL 1) (Fig. 4K).
424 There was an increase in S100A4$^+$ and α-smooth muscle actin (α-SMA$^+$) CAF populations in
425 CRD-induced tumors compared to those in LD tumors (Fig. 4L).
426 Our data suggest that CRD enhances tumor progression and lung metastasis by enhancing the
427 immunosuppressive microenvironment and increasing the CSC population. Our scRNA-seq, and
428 immunostaining results confirmed the "cold" characteristics of CRD tumors. The gating strategy
429 used for flow cytometry is shown in Fig. S7**.** Chemokines play a pivotal role in the migration
430 pattern of immune cells into the tumor and facilitate the immunosuppressive TME by enhancing
431 the differentiation and infiltration of immunosuppressive cells, such as T_{reg} cells, myeloid-derived
432 suppressor cells (MDSCs), and tumor-associated macrophages (TAMs). To investigate whether
433 CRD altered the chemokine-cytokine network in the studied mice, we quantified the levels of 40
434 circulating chemokines in the plasma of LD and CRD mice using a Proteome Profiler. Marked
435 increases in circulating IFN-γ, IL-1β, G-CSF, and IL-16 levels were observed in CRD mice (Fig.
436 S8A). As plasma cytokine/chemokine levels do not represent the TME, we used the data from our
437 scRNA-seq and real-time PCR to assess chemokine/cytokine network expression levels in LD and
438 CRD tumors. Levels of specific cytokines/chemokines known to favor an immunosuppressive
439 microenvironment (Vilgelm and Richmond 2019), such as CCL12 (Fig. 4M) and CXCL5 (Fig.
440 4N), were upregulated in CRD-induced GEMM tumors. Levels of CCL28, known to induce T_{reg}
441 infiltration and create an immunosuppressive environment (Yang 2017), were upregulated in CRD
442 tumors, as shown using scRNA-seq (Fig. S8B), but not significantly, as shown using real-time

443 PCR (Fig. S8C). Levels of IL-17β and IL10, were upregulated modestly (but not significantly) in
444 CRD-induced 4T1 tumors (Fig. S8C).
445
446 **Malignant human breast cancer cells have high CRD**
447 Earlier studies (Hadadi 2020) and the present study used GEMMs to investigate the effect of CRD
448 on tumorigenesis. However, more insights are needed into the molecular mechanisms underlying
449 CRD at the single-cell level and in human tumors. To investigate the process underlying CRD
450 during mammary tumorigenesis, we used a scRNA sequence dataset from a previously published
451 study (Wu, Al-Eryani et al. 2021). The dataset included TNBC, HER2-positive, and luminal
452 tumors. Using large-scale copy number variation (CNV) from the transcriptomics data (Tirosh,
453 Izar et al. 2016), we separated definitive malignant cells from potential nonmalignant cell
454 populations in TNBC (Fig. 5A), luminal (ER^+/PR^+) (Fig. S9A), and HER2 tumors (Fig. S9B).
455 Based on a previous study (He, Fan et al. 2022), the CRD score was calculated using the expression
456 of 358 circadian-related genes (He, Fan et al. 2022). Next, we quantified the CRD scores of
457 malignant (and nonmalignant) cells in different types of human breast tumors. Aggressive TNBC
458 comprised significantly ($P < 0.01$) more malignant cells with high CRD scores (Fig. 5B) than
459 luminal tumors (Fig. S9C)**.** Malignant cells in HER2 tumors also showed a high CRD score (Fig
460 S9D). *Cry1*, *Per1*, and *Per2* expression decreased in TNBC malignant cells compared to non-
461 malignant cells, as shown using the scRNA-seq dataset (Fig. 5C). To define the role of CRD in
462 large patient populations, we used publicly available RNA-seq data from tumors (N=1104 patients)
463 and surrounding tissues (N = 113) of patients with breast cancer in The Cancer Genome Atlas
464 (TCGA). The expression of core clock genes (*Per1*, *Per2*, *Per3*, *Cry2*, *Rorc*, *Rorb*, *Nr1d1*, and

465 *Arnt2*) was significantly ($P < 0.05$) lower in the tumors than in the surrounding tissues (Fig. 5D).
466 These data suggest that the core clock is disrupted in human breast tumors.

467 **CRD creates "cold" tumors by inducing LILRB4 expression**

468 Next, to identify the molecular mechanism that regulates the CRD-induced immunosuppressive
469 TME, we searched for transcripts differentially expressed between the samples (mammary tumors
470 and glands) collected from mice exposed to ordinary light and dark conditions (LD 12:12) and
471 mice subjected to CRD. Differential gene expression (DGE) analysis of our scRNA-seq data
472 revealed that LILRB4 was upregulated in the tumor samples from CRD-induced GEMMs (Fig.
473 6A, S10A). LILRB4, an immunoreceptor tyrosine-based inhibitory motif-containing receptor,
474 suppresses T-cell activity via a signaling pathway involving apolipoprotein E (APOE), SH2-
475 domain-containing protein tyrosine phosphatase-2 (SHP-2), urokinase-like plasminogen activator
476 (uPAR or Plaur), and arginase 1 (ARG-1) (Sharma 2021). Recent studies have shown that LILRB4
477 creates an immunosuppressive microenvironment in AML (Deng, Gui et al. 2018) and solid
478 cancers (Sharma 2021) by inhibiting $CD8^+$ T-cell infiltration and inducing T_{reg}. Real-time PCR
479 showed that CRD enhanced LILRB4 levels significantly in the CRD-induced GEMM tumors (Fig.
480 6B), and CRD-induced 4T1 tumors (Fig. 6C). The immunofluorescence analysis showed an
481 elevation of ARG1 expression in CRD-induced GEMM tumors (Fig. 6D). The transcript level of
482 ARG1 was significantly increased in CRD-induced tumors (Fig. 6E). Increased LILRB4
483 expression enhanced the immunosuppressive TME as CD8+ T cell infiltration decreased, whereas
484 M2- macrophage (CD163) and T_{reg} (FOXP3) populations increased in CRD-induced mammary
485 tumors from GEMMs, as shown using immunofluorescence assay (Fig. 6F). Furthermore, LILRB4
486 transcript levels were significantly increased in CRD-induced mammary glands (Fig. 6G).
487 Mammary gland LILRB4 transcript levels exhibited robust diurnal oscillations, increasing during

488 the light phase under normal and dark conditions. Under CRD, the amplitude of this rhythm was
489 dampened, but the phase was reserved (or only slightly shifted), and the transcript level peaked
490 during the dark phase (Fig. S10B). The transcript level of ARG1 increased modestly but non-
491 significantly in the CRD-induced mammary glands (Fig. S10C). The transcript level of the
492 chemokine CCL12 increased significantly in CRD-induced mammary glands (Fig. S10D). The
493 transcript level of CXCL5 is raised modestly but not significantly in CRD-induced mammary
494 glands (Fig. S10E). Overall, these changes in the immune milieus of the CRD-induced mammary
495 microenvironment can decrease adaptive immunity and enhance susceptibility to cancer and other
496 diseases.
497 To investigate whether LILRB4 expression was responsible for creating an immunosuppressive
498 TME, we explored the effects of LILRB4-immunotherapy on tumor progression in CRD mice by
499 treating them with an LILRB4 antibody (Sharma 2021). Briefly, 4T1 cells were orthotopically
500 transplanted into BALB/cJ mice to develop TNBC tumors. Four to five days (~4-5) days after the
501 transplantation, once palpable tumors developed, mice were placed into LD or CRD condition.
502 The LILRB4 antibody was administered on days 6, 9, and 12 after developing palpable tumors.
503 Mice were sacrificed 3 weeks after the development of palpable tumors (day 21) (Fig. 6H), and
504 lung metastasis and the TME were examined. We observed a significant decrease ($P<0.0001$) in
505 the prevalence of lung metastasis in LILRB4-antibody treated mice under CRD condition (Fig.
506 6I). Flow cytometric analysis showed an inhibition of the T_{reg} cell population in LILRB4-antibody
507 treated tumors under CRD condition, which alleviate the immunosuppressive microenvironment
508 (Fig. 6J). LILRB4-targeted therapy inhibited ARG1 transcript level (Fig. 6K) in CRD-induced
509 tumors. We also observed a modest but non-significant decrease in CCL12 (Fig. S10F) and CXCL5
510 (Fig. S10G) transcript levels in CRD-induced tumors. No significant difference was observed in

511 the number of lung metastasis foci in LD mice treated with the LILRB4-antibody (Fig S10H).
512 LILRB4-antibody treatment under LD conditions does not decrease the T_{reg} population (Fig. S10I),
513 ARG1 transcript level (Fig. S10J), and the chemokines (CCL12, CXCL5) (Fig. S10K, L)
514 significantly. These findings fortify the notion that elevated LILRB4 contributes to CRD-induced
515 aggressive tumorigenesis.
516
517 **Discussion**
518 Following the chronic jet lag protocol, here, we showed that CRD interrupted the biological clock,
519 affected the mammary gland morphology, and accelerated aggressive basal mammary
520 tumorigenesis and lung metastasis by altering the TME. CRD induced an immunosuppressive
521 TME and turned the tumors "cold." Malignant human breast cancer cells were shown to have high
522 CRD scores. We also identified the molecular mechanisms underlying CRD-induced aggressive
523 mammary tumorigenesis: CRD created "cold" tumors by inducing LILRB4 expression.
524 CRD-induced mammary glands exhibited underdeveloped (and abnormal) TEBs and
525 reduced branching morphology. CRD-induced mice showed mammary gland ductal hyperplasia,
526 which can be the early sign of ductal cancer (Behbod, Gomes et al. 2018), as seen by H&E and
527 Ki67 staining. This indicates the role of the circadian clock in mammary gland development and
528 the potential role of CRD in breast cancer initiation. Our study showed that CRD accelerated
529 spontaneous mammary tumor initiation and lung metastasis but not tumor progression, indicating
530 that CRD affects the early events of tumor initiation, rather than the growth of the established
531 tumors. LILRB4 expression was increased in mammary glands and CRD-induced mammary
532 tumors, revealing an unidentified mechanism responsible for CRD-induced tumorigenesis, lung
533 metastasis, and mammary gland development. The jet lag protocol used here mimics the effects of

534 rotating shift work or frequent eastbound trans-meridian flights and has been previously shown to
535 cause severe perturbations of circadian rhythmicity (Papagiannakopoulos, Bauer et al. 2016,
536 Hadadi, Taylor et al. 2020, Pariollaud, Ibrahim et al. 2022). Consistent with the results of published
537 studies (Pariollaud, Ibrahim et al. 2022), we found that CRD affected the rhythmicity of many
538 clock genes (e.g., *Clock, Bmal1, Per1*, and *Cry1*) in the mammary glands; however, *Per2*
539 expression remained rhythmic after CRD, indicating that *Per2* is more sensitive to phase
540 entrainment signals of molecular oscillators in peripheral tissues.

541 Using scRNA-seq and TCGA data, we showed that the expression of certain circadian
542 genes was decreased in aggressive human TNBCs compared with that in the surrounding
543 mammary tissues. Our analysis also revealed that the malignant cells in aggressive human TNBCs
544 had higher CRD scores and downregulated *PER1*, *PER2*, and *CRY1* significantly than
545 nonmalignant cells.

546 Our study showed that CRD induced an immunosuppressive tumor microenvironment,
547 which could be involved in increased tumor burden in mice maintained under the CRD schedule.
548 The TME consists of natural killer cells, $CD8^+$ T cells, $CD4^+$ helper T (T_h) cells, proinflammatory
549 macrophages (M1), and DCs, which elicit antitumor immune responses, whereas the presence of
550 MDSCs and $FOXP3^+$ T_{reg} counteracts tumor immunity (Labani-Motlagh, Ashja-Mahdavi et al.
551 2020). Our scRNA-seq study, and FACS showed that CRD decreased cytotoxic T-cell infiltration,
552 and the DC population. This supports the recent finding that DC and T-cell-autonomous circadian
553 clocks are responsible for time-of-the-day-dependent antitumor effects (Wang, Barnoud et al.
554 2023). CRD-induced $S100a4^+$ CAF, and α-SMA^+ CAF populations are known to promote tumor
555 progression and metastasis and contribute to an immunosuppressive TME (Costa, Kieffer et al.
556 2018). We found an increase in the M2 macrophage, and MDSC population and a decrease in the

557 M1 macrophage population in CRD tumors. M2 macrophages play a significant role in creating
558 an immunosuppressive microenvironment (Hao, Lu et al. 2012), whereas M1 macrophages induce
559 inflammation and kill tumor cells (Hao, Lu et al. 2012, Pan, Yu et al. 2020). MDSCs are also
560 known to create an immunosuppressive environment by suppressing T-cell responses and $CD8^+$ T-
561 cell infiltration (Li, Shi et al. 2021). Our FACS results corroborated the scRNA-seq results and
562 confirmed that CRD enhanced the T_{reg} population. CRD increased the leukocyte ($CD45^+$)
563 population, corroborating that the jet lag schedule enhances leukocyte levels in melanoma (Aiello,
564 Fedele et al. 2020). Our scRNA-seq and real-time PCR studies showed that CRD induced a pro-
565 tumorigenic and immunosuppressive microenvironment by increasing the expression of CCL12
566 and CXCL5. The upregulation of CCL12 (human orthologs of CCL2) (Yang J 2020) and CXCL5
567 reportedly lead to the accumulation of MDSCs (Li, Shi et al. 2021). CRD also enhances CCL28
568 production, which leads to the recruitment of T_{reg} cells in the TME (Ren, Yu et al. 2016).

569 We further demonstrated that CRD enhanced the expression of LILRB4 *in vivo* in healthy
570 mammary glands and mammary tumors. Recent studies have shown that LILRB4 creates an
571 immunosuppressive microenvironment in AML (Deng, Gui et al. 2018) and solid cancers (Sharma
572 2021) by inhibiting $CD8^+$ T-cell infiltration and inducing T_{reg}. LILRB4 inhibited the differentiation
573 of $CD8^+$ and $CD4^+$ T cells (Deng, Gui et al. 2018). By activating the JAK/STAT signaling pathway,
574 LILRB4 controls the expression of cytokines in macrophages (Truong, Hong et al. 2019). In
575 different malignant cancers, LILRB4 expression in MDSCs is associated with decreased survival
576 in patients (de Goeje, Bezemer et al. 2015). A recent study showed that LILRB4 blockade
577 increased the proportions of tumor immune infiltrates, effector (T_{eff}) levels, and altered the TME
578 toward reduced immunosuppression in solid tumors (Sharma 2021). Together, these findings
579 reveal that LILRB4 creates an immunosuppressive microenvironment, thereby decreasing its

580 antitumor efficacy. Our study showed that CRD activated LILRB4 signaling in healthy mammary
581 glands and aggressive TNBCs. Using real-time PCR and immunofluorescence analysis, we
582 observed increased *ARG1* expression in CRD-induced tumors. Analysis of the TME using
583 multiplexing immunostaining showed an immunosuppressive microenvironment as the cytotoxic
584 T-cell and M1 macrophage populations decreased. In contrast, T_{reg}, and M2 macrophage
585 populations were increased in CRD tumors. We found that the disruption of circadian rhythm
586 upregulated LILRB4 expression, which correlated with mammary tumor progression and
587 abnormal morphology in the mammary glands.

588 CRD upregulated the expression of immunosuppressive chemokines (CCL12) in mouse
589 mammary glands. CCL2 (an orthologous of mouse CCL12) increases stromal density and elevates
590 cancer risk (Sun, Glynn et al. 2017). An immunosuppressive environment can increase
591 susceptibility to opportunistic infections (Shu Kurizky, Dos Santos Neto et al. 2020) in CRD-
592 induced patients. This study demonstrated how an inhibitory immune receptor altered the TME
593 and influenced aggressive mammary tumorigenesis in response to CRD. We showed that the
594 targeted LILRB4 immunotherapy reduced CRD-induced lung metastasis by inhibiting
595 immunosuppressive TME.

596 Our findings suggest that LILRB4 is a potential therapeutic target for mitigating CRD-
597 induced cancer risk in populations exposed to chronic CRD, such as shift workers. LILRB4
598 inhibition was also found to improve the immunosuppressive microenvironment. However, how
599 the disruption of the cell-autonomous molecular clock by CRD could enhance LILRB4 expression
600 remains unknown. Further investigations are needed to determine why and how CRD enhances
601 LILRB4 expression. Additional investigations are required to determine whether the chronic

elevation of LILRB4 levels in the mammary glands in response to CRD occurs early in the disease process and whether LILRB4 is present in other anatomical locations.

In conclusion, our study provides the link between CRD and aggressive basal mammary tumorigenesis, metastasis, and abnormal mammary gland morphology. Based on our data, we propose a signaling cascade (**Fig. 7)** as a possible mechanism behind CRD-induced mammary gland disruption, enhanced aggressive tumorigenesis, lung metastasis, and immunosuppressive TME.

List of abbreviations:

LD	Light and Dark
CRD	Circadian Rhythm Disruption
LILRB4	leukocyte immunoglobulin-like receptor 4
TNBC	Triple-negative Breast Cancer
ER	Estrogen receptor
PR	Progesterone receptor
HER2	Human Epidermal Growth Factor Receptor 2
SCN	Suprachiasmatic nucleus
CLOCK	Circadian locomotor output cycles kaput
BMAL-1	Brain and muscle Arnt-like protein-1
PAS	Per-Arnt-Sim domain
PER	Period
CRY	Cryptochrome
TME	Tumor microenvironment
GEMM	Genetically engineered mouse model
FVB	Friend LeukemiaVirus B
TEB	Terminal end bud
H&E	Hematoxylin and Eosin
AGR	Albumin-to-globulin ratio
scRNA-seq	Single-cell RNA sequence

CD	Cluster of differentiation
KLF2	Krüppel-like factors2
SLC2A1	Solute Carrier Family 2 Member 1
TRPS1	Transcriptional Repressor GATA Binding 1
TOP2A	Topoisomerase II Alpha
FTH1	Ferritin heavy chain 1
NES	Nestin
CLEC11A	C-Type Lectin Domain Containing 11A
S100A4	S100 Calcium Binding Protein A4
RPL35A	Ribosomal Protein L35a
FXYD3	FXYD Domain Containing Ion Transport Regulator 3
COL1A2	Collagen Type I Alpha 2 Chain
EPCAM	Epithelial cellular adhesion molecule
CDK	Cyclin-dependent kinase
M1	Type1 macrophage
M2	Type2 macrophage
CAFs	Cancer-associated fibroblasts
L-R	Ligand-receptor
FGF	Fibroblast growth factor
PDGF	Platelet-derived growth factor
TNF	Tumor necrosis factor
NOTCH	Neurogenic locus notch homolog protein
TGFβ	transforming growth factor-beta
CoA	Coenzyme A
MxIF	Multiplex immunofluorescence
Treg	Regulatory T-cell
α-SMA	Alpha-smooth muscle actin
FN1	fibronectin 1
FACS	Fluorescence-activated cell sorting
FoxP3	forkhead box P3
CSC	Cancer stem cell

MDSCs	Myeloid-derived suppressor cells
TAMs	Tumor-associated macrophages
IFN	Interferon
IL	Interleukin
G-CSF	Granulocyte colony-stimulating factor
CCL2/12	Chemokine (C-C motif) ligand 2/12
CXCL5	C-X-C motif chemokine 5
PCR	Polymerase chain reaction
TCGA	The Cancer Genome Atlas
DGE	Differential gene expression
APOE	apolipoprotein E
SHP-2	SH2 domain-containing protein tyrosine phosphatase-2
uPAR	Urokinase-like plasminogen activator
ARG1	Arginase 1
AML	Acute Myeloid Leukemia
mIHC	multiplex immunofluorescence histochemistry
ARNT2	Aryl hydrocarbon receptor nuclear translocator 2
NR1D1	Nuclear Receptor Subfamily 1 Group D Member 1
RORB & C	RAR Related Orphan Receptor B and C
ITIMs	Immunoreceptor tyrosine-based inhibitory motifs
ITAMs	Immunoreceptor tyrosine-based activating motifs
APCs	Antigen-presenting cells
JAK/STAT	Janus kinase/signal transducers and activators of transcription

Availability of data and materials

All data needed to evaluate the conclusions in the paper are present in the paper and/or the Supplementary Materials.

Competing interests: Authors declare that they have no competing interests.

Funding: This work was funded by the Texas A&M University Faculty Development Grant (to T.R.S) and Strategic Transformative Research Funds (STRP to TRS), NIH grant NIH 5 P01HL160471 (to A.K) and NIH R01NS131628 (to A.K), NIH R35GM151020 (to J.J), and NSF CCF-1934904 (to B.M).

Author contributions: Conceptualization: T.R.S. Methodology: O.O., M.S., A.C, D.J.B., T.N., D.F., Y.J-H., J.J and T.R.S. Investigation: O.O., M.S., A.C, D.J.B., T.N.,C.,N., T.R.S. Visualization: O.O, M.S., D.F., YJ-H., T.R.S. Supervision: T.R.S. Analysis of data: T.R.S., B.M., J.J., A.K. Writing—original draft: O.O., M.S., T.R.S. Review and editing: A.K., B.M., L.F and J.J.

Acknowledgments
We thank Dr. Mahul Chakraborty for helping with real-time PCR, Dr. Gus Wright for helping with flow cytometry experiments and analysis, histology core facility (Texas A&M University) for histology work, Ashley Nguyen, David Arreola, Subiksha Sankar, and Aaryan Amin for helping with circadian cabinets.

Reference:

Ai, D., et al. (2021). "TRPS1: a highly sensitive and specific marker for breast carcinoma, especially for triple-negative breast cancer." Modern Pathology **34**(4): 710-719.

Aiello, I., et al. (2020). "Circadian disruption promotes tumor-immune microenvironment remodeling favoring tumor cell proliferation." Sci Adv **6**(42).

Alluri, P. and L. A. Newman (2014). "Basal-Like and Triple-Negative Breast Cancers: Searching for Positives Among Many Negatives." Surgical Oncology Clinics of North America **23**(3): 567-577.

Almansour, N. M. (2022). "Triple-Negative Breast Cancer: A Brief Review About Epidemiology, Risk Factors, Signaling Pathways, Treatment and Role of Artificial Intelligence." Front Mol. Biosci **9**.

Anders, C. and L. A. Carey (2008). "Understanding and treating triple-negative breast cancer." Oncology (Williston Park) **22**(11): 1233-1239; discussion 1239-1240, 1243.

Baker, S. J., et al. (2022). "CDK4: a master regulator of the cell cycle and its role in cancer." Genes Cancer **13**: 21-45.

Battaglin, F., et al. (2021). "Clocking cancer: the circadian clock as a target in cancer therapy." Oncogene **40**(18): 3187-3200.

735
736 Behbod, F., et al. (2018). "Modeling Human Ductal Carcinoma In Situ in the Mouse." J Mammary
737 Gland Biol Neoplasia **23**(4): 269-278.

738
739 Bernal, A. and L. Arranz (2018). "Nestin-expressing progenitor cells: function, identity and
740 therapeutic implications." Cell Mol Life Sci **75**(12): 2177-2195.

741
742 Binnewies, M., et al. (2018). "Understanding the tumor immune microenvironment (TIME) for
743 effective therapy." Nat Med **24**(5): 541-550.

744
745 Blakeman, V., et al. (2016). "Circadian clocks and breast cancer." Breast Cancer Res **18**(1): 89.

746
747 Casiraghi, L. P., et al. (2012). "Forced Desynchronization of Activity Rhythms in a Model of
748 Chronic Jet Lag in Mice." Journal of Biological Rhythms **27**(1): 59-69.

749
750 CDC (2015). "Work Organization Characteristics (NHIS 2015) Charts; National Health Interview
751 Survey (NHIS 2015)." https://wwwn.cdc.gov/Niosh-whc/chart/OHS-
752 WORKORG?OU=*&T=OU&V=R.

753
754 Chun, S. K., et al. (2022). "Disruption of the circadian clock drives Apc loss of heterozygosity to
755 accelerate colorectal cancer." Science Advances **8**(32): eabo2389.

756
757 Costa, A., et al. (2018). "Fibroblast Heterogeneity and Immunosuppressive Environment in
758 Human Breast Cancer." Cancer Cell **33**(3): 463-479.e410.

759
760 de Goeje, P. L., et al. (2015). "Immunoglobulin-like transcript 3 is expressed by myeloid-derived
761 suppressor cells and correlates with survival in patients with non-small cell lung cancer."
762 OncoImmunology **4**(7): e1014242.

763
764 Deng, M., et al. (2018). "LILRB4 signalling in leukaemia cells mediates T cell suppression and
765 tumour infiltration." Nature **562**(7728): 605-609.

766
767 Elston, C. W. and I. O. Ellis (2002). "Pathological prognostic factors in breast cancer. I. The value
768 of histological grade in breast cancer: experience from a large study with long-term follow-up."
769 Histopathology **41**(3A): 154-161.

770
771 Fei, F., et al. (2017). "Role of metastasis-induced protein S100A4 in human non-tumor
772 pathophysiologies." Cell Biosci **7**: 64.

773
774 Finak, G., et al. (2015). "MAST: a flexible statistical framework for assessing transcriptional
775 changes and characterizing heterogeneity in single-cell RNA sequencing data." Genome Biology
776 **16**(1): 278.

777
778 Grosche, L., et al. (2020). "The CD83 Molecule - An Important Immune Checkpoint." Front
779 Immunol **11**: 721.

780
781 Hadadi, E., et al. (2020). "Chronic circadian disruption modulates breast cancer stemness and
782 immune microenvironment to drive metastasis in mice." Nature Communications **11**(1): 3193.

783
784 Hadadi, E., Taylor, W., Li, X. M., Aslan, Y., Villote, M., Rivière, J., Duvallet, G., Auriau, C., Dulong,
785 S., Raymond-Letron, I., Provot, S., Bennaceur-Griscelli, A., & Acloque, H. (2020). "Chronic
786 circadian disruption modulates breast cancer stemness and immune microenvironment to drive
787 metastasis in mice." Nature communications **11**(1).

788
789 Han, C., et al. (2020). "Biomarkers for cancer-associated fibroblasts." Biomark Res **8**(1): 64.

790
791 Hao, N. B., et al. (2012). "Macrophages in tumor microenvironments and the progression of
792 tumors." Clin Dev Immunol **2012**: 948098.

793
794 Hao, Y., et al. (2021). "Integrated analysis of multimodal single-cell data." Cell **184**(13): 3573-
795 3587.e3529.

796
797 He, J., et al. (2017). "Prognostic Effect of Albumin-to-Globulin Ratio in Patients with solid
798 tumors: A Systematic Review and Meta-analysis." J Cancer **8**(19): 4002-4010.

799
800 He, L., et al. (2022). "Single-cell transcriptomic analysis reveals circadian rhythm disruption
801 associated with poor prognosis and drug-resistance in lung adenocarcinoma." J Pineal Res **73**(1):
802 e12803.

803
804 Hemmer, A., et al. (2021). "The Effects of Shift Work on Cardio-Metabolic Diseases and Eating
805 Patterns." Nutrients **13**(11).

806
807 Kelleher, F. C., et al. (2014). "Circadian molecular clocks and cancer." Cancer Lett **342**(1): 9-18.

808

809 Kersemans, V., et al. (2013). "Subcutaneous tumor volume measurement in the awake,
810 manually restrained mouse using MRI." Journal of Magnetic Resonance Imaging **37**(6): 1499-
811 1504.

812

813 Labani-Motlagh, A., et al. (2020). "The Tumor Microenvironment: A Milieu Hindering and
814 Obstructing Antitumor Immune Responses." Front Immunol **11**: 940.

815

816 Lee, S., et al. (2010). "Disrupting circadian homeostasis of sympathetic signaling promotes
817 tumor development in mice." PLoS One **5**(6): e10995.

818

819 Li, K., et al. (2021). "Myeloid-derived suppressor cells as immunosuppressive regulators and
820 therapeutic targets in cancer." Signal Transduction and Targeted Therapy **6**(1): 362.

821

822 Li, M., et al. (2023). "FXYD3 functionally demarcates an ancestral breast cancer stem cell
823 subpopulation with features of drug-tolerant persisters." J Clin Invest **133**(22).

824

825 Maroulakou, I. G., et al. (1994). "Prostate and mammary adenocarcinoma in transgenic mice
826 carrying a rat C3(1) simian virus 40 large tumor antigen fusion gene." Proc Natl Acad Sci U S A
827 **91**(23): 11236-11240.

828

829 Merrick, D., et al. (2019). "Identification of a mesenchymal progenitor cell hierarchy in adipose
830 tissue." Science **364**(6438).

831

832 Meyer, J. S., et al. (2011). "Optic vesicle-like structures derived from human pluripotent stem
833 cells facilitate a customized approach to retinal disease treatment." Stem Cells **29**(8): 1206-
834 1218.

835

836 Moreira, A. C., et al. (2022) H-Ferritin Produced by Myeloid Cells Is Released to the Circulation
837 and Plays a Major Role in Liver Iron Distribution during Infection. International Journal of
838 Molecular Sciences **23**, DOI: 10.3390/ijms23010269

839

840 Neubauer, E., et al. (2016). "Comparative evaluation of three proliferation markers, Ki-67,
841 TOP2A, and RacGAP1, in bronchopulmonary neuroendocrine neoplasms: Issues and prospects."
842 Oncotarget **7**(27): 41959-41973.

843

844 Pan, Y., et al. (2020). "Tumor-Associated Macrophages in Tumor Immunity." Front Immunol **11**:
845 583084.

846

847 Panda, S., et al. (2002). "Coordinated transcription of key pathways in the mouse by the
848 circadian clock." Cell **109**(3): 307-320.

849

850 Papagiannakopoulos, T., et al. (2016). "Circadian Rhythm Disruption Promotes Lung
851 Tumorigenesis." Cell Metabolism **24**(2): 324-331.

852

853 Pariollaud, M., et al. (2022). "Circadian disruption enhances HSF1 signaling and tumorigenesis in
854 Kras-driven lung cancer." Science Advances **8**(39): eabo1123.

855

856 Ren, L., et al. (2016). "Hypoxia-induced CCL28 promotes recruitment of regulatory T cells and
857 tumor growth in liver cancer." Oncotarget **7**(46): 75763-75773.

858

859 Ren, X., et al. (2022). "Immunological Classification of Tumor Types and Advances in Precision
860 Combination Immunotherapy." Front Immunol **13**: 790113.

861

862 Rodriguez de la Fuente, L., et al. (2021). "Tumor dissociation of highly viable cell suspensions for
863 single-cell omic analyses in mouse models of breast cancer." STAR Protoc **2**(4): 100841.

864

865 Sangwung, P., et al. (2017). "KLF2 and KLF4 control endothelial identity and vascular integrity."
866 JCI Insight **2**(4): e91700.

867

868 Schernhammer, E. S., et al. (2001). "Rotating night shifts and risk of breast cancer in women
869 participating in the nurses' health study." J Natl Cancer Inst **93**(20): 1563-1568.

870

871 Schmid, B., et al. (2011). "A New ImageJ Plug-in “ActogramJ” for Chronobiological Analyses."
872 Journal of Biological Rhythms **26**(5): 464-467.

873

874 Sharma, N., Atolagbe, O., Ge, Z., Allison, J (2021). "LILRB4 suppresses immunity in solid tumors
875 and is a potential target for immunotherapy." J of Exp Medicine **218**(7).

876

877 Shu Kurizky, P., et al. (2020). "Opportunistic tropical infections in immunosuppressed patients."
878 Best Pract Res Clin Rheumatol **34**(4): 101509.

879

880 Stephenson, E. M., et al. (2021). "Cancer clocks in tumourigenesis: the p53 pathway and
881 beyond." Endocrine-Related Cancer **28**(4): R95-R110.

882

883 Storch, K. F., et al. (2002). "Extensive and divergent circadian gene expression in liver and heart."
884 Nature **417**(6884): 78-83.

885

886 Strobl, H., et al. (1998). "Identification of CD68+lin− Peripheral Blood Cells with Dendritic
887 Precursor Characteristics1." The Journal of Immunology **161**(2): 740-748.

888

889 Sun, X., et al. (2017). "CCL2-driven inflammation increases mammary gland stromal density and
890 cancer susceptibility in a transgenic mouse model." Breast Cancer Res **19**(1): 4.

891

892 Tirosh, I., et al. (2016). "Dissecting the multicellular ecosystem of metastatic melanoma by
893 single-cell RNA-seq." Science **352**(6282): 189-196.

894

895 Truong, A. D., et al. (2019). "Characterization and functional analyses of novel chicken leukocyte
896 immunoglobulin-like receptor subfamily B members 4 and 5." Poult Sci **98**(12): 6989-7002.

897

898 Trzpis, M., et al. (2007). "Epithelial cell adhesion molecule: more than a carcinoma marker and
899 adhesion molecule." Am J Pathol **171**(2): 386-395.

900

901 Usary, J., Darr, UB., Pfefferle, A, Perou, C. (2017). "Genetically Engineered Mouse Models of
902 Distinct Breast Cancer Subtypes." Curr Protoc Pharmacol **72**(14): 38.31-38.11.

903

904 Van Dycke, K. C. G., et al. (2015). "Chronically Alternating Light Cycles Increase Breast Cancer
905 Risk in Mice." Current biology : CB **25**(14): 1932-1937.

906

907 Vilgelm, A. E. and A. Richmond (2019). "Chemokines Modulate Immune Surveillance in
908 Tumorigenesis, Metastasis, and Response to Immunotherapy." Frontiers in Immunology **10**.

909

910 Vitaterna, M. H., et al. (2019). "Genetics of Circadian Rhythms." Neurol Clin **37**(3): 487-504.

911

912 Wang, C., et al. (2023). "Dendritic cells direct circadian anti-tumour immune responses." Nature
913 **614**(7946): 136-143.

914

915 Wang, Y., et al. (2023). "Cell death-related biomarker SLC2A1 has a significant role in prognosis
916 prediction and immunotherapy efficacy evaluation in pan-cancer." Frontiers in Genetics **13**.

917

918 Wu, S. Z., et al. (2021). "A single-cell and spatially resolved atlas of human breast cancers."
919 Nature genetics **53**(9): 1334-1347.

920
921 Wu, T., et al. (2021). "clusterProfiler 4.0: A universal enrichment tool for interpreting omics
922 data." The Innovation **2**(3): 100141.

923
924 Yang J, A. M., Ling S, Teitz-Tennenbaum S, Zemans RL, Osterholzer JJ, Sisson TH, Kim KK. (2020).
925 "Diverse Injury Pathways Induce Alveolar Epithelial Cell CCL2/12, Which Promotes Lung
926 Fibrosis." Am J Respir Cell Mol Biol. **62**(5): 622-632.

927
928 Yang, Z., L., Liu, K.Y., Lin, F.J., Shi, H.M., Ou, Z.L. (2017). "CCL28 promotes breast cancer growth
929 and metastasis through MAPK-mediated cellular anti-apoptosis and pro-metastasis." Oncology
930 Reports **38**(3): 1393-1401.

931
932 Yuan, X., et al. (2018). "Night Shift Work Increases the Risks of Multiple Primary Cancers in
933 Women: A Systematic Review and Meta-analysis of 61 Articles." Cancer Epidemiol Biomarkers
934 Prev **27**(1): 25-40.

935

936
937

938 **Figures**

939

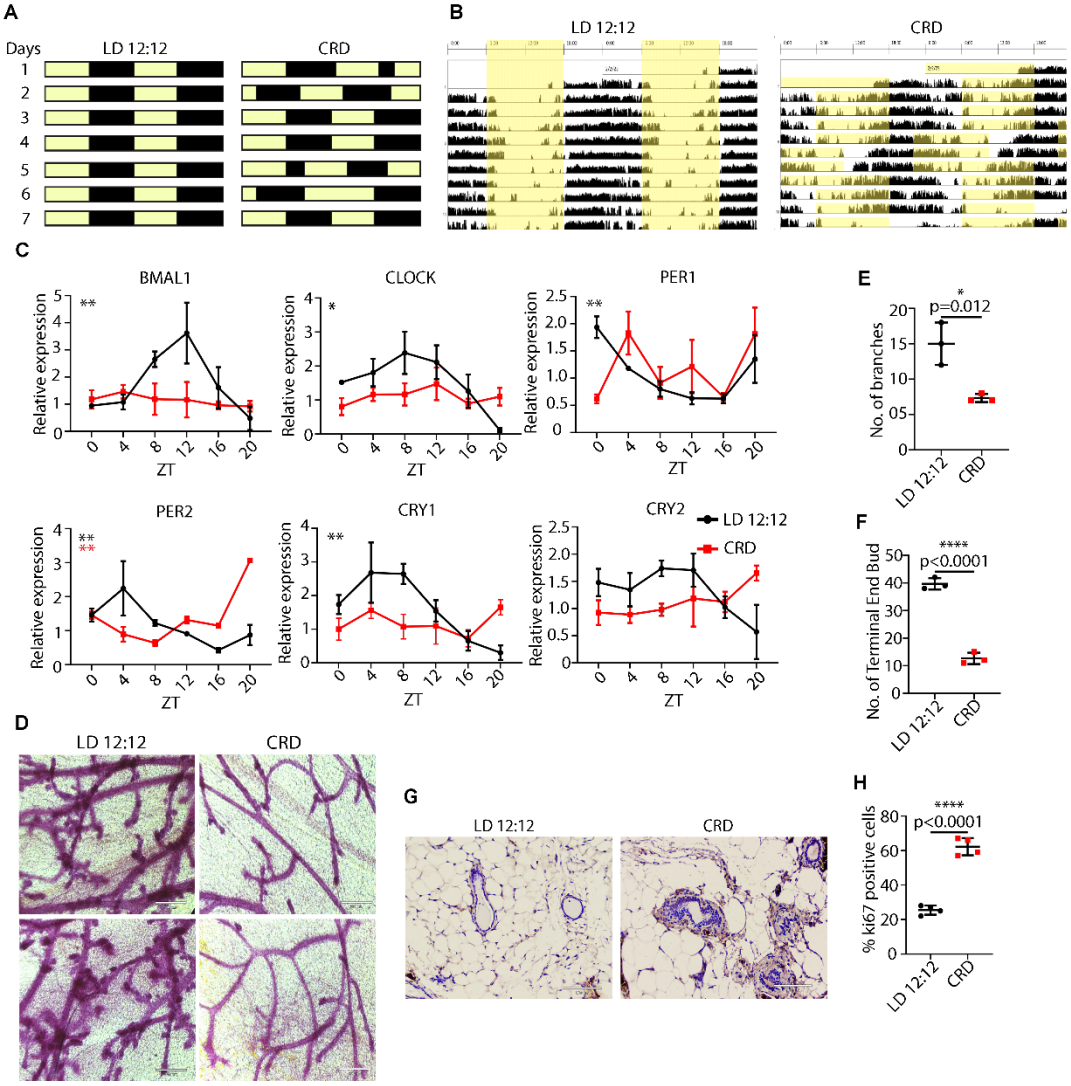

940

941 **Fig. 1. CRD severely impairs rhythmicity and disrupts mammary gland morphogenesis. (A)**
942 Schematic representation of the CRD protocol. **(B)** FVB female mice were housed under LD 12:12
943 or CRD for 8 weeks. Representative actograms of LD and CRD mice. LD: 12 h light and 12 h
944 dark; CRD: circadian rhythm disruption using jet lag protocol, represented by a shortening of the
945 dark period by 8 h every third day. **(C)** Mammary glands were collected at the indicated times.
946 Gene expression normalized to GAPDH expression was measured using quantitative real-time
947 PCR data represented as mean ± SEM for n=3 females per time point and light condition.
948 Rhythmicity was determined using JTK_Cycle analyses; **P*JTKcycle < 0.05, ***P*JTKcycle <
949 0.01, ****P*JTKcycle < 0.001, and *****P*JTKcycle < 0.0001. CRD disrupts branching
950 morphogenesis in WT virgin FVB mice. **(D, E, F)** Representative images of branching and
951 development of terminal ducts in LD and CRD animals are shown in LD and CRD-induced
952 mammary glands **(D, E, F)**, scale bar: 350 µm, (**P* < 0.05, error bars indicate SEM, n = 3). **(G)**
953 The effect of CRD on mammary ductal hyperplasia is shown by hematoxylin and eosin (H&E)
954 staining of the mammary gland (**G**) and by using Ki67 **(H)** of the mammary glands. Scale bar: 100
955 µm.

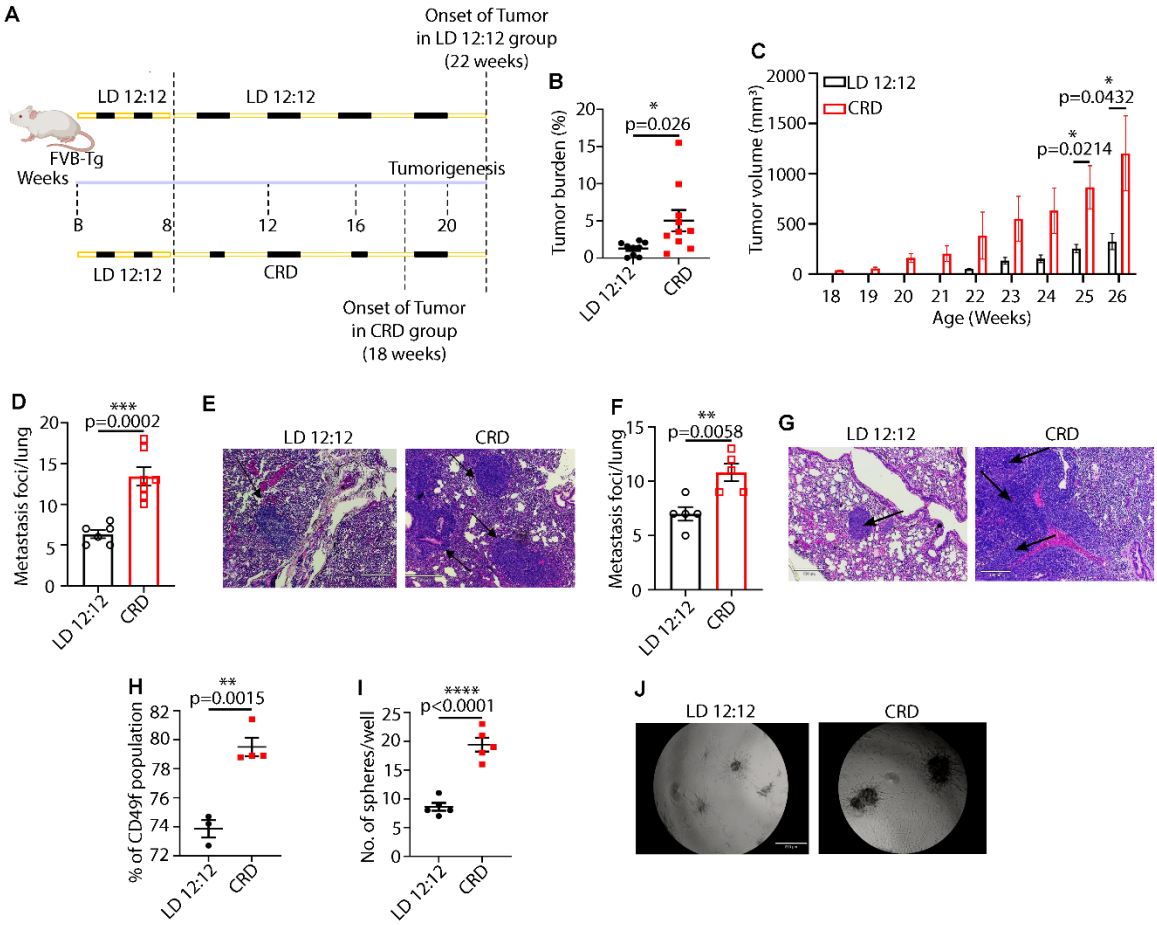

Fig. 2. CRD increases aggressive mammary tumorigenesis and lung metastasis. Experimental timeline for evaluation of the effect of CRD on spontaneous TNBC in (FVB-Tg(C3-1-TAg)cJeg (C3-TAg) mice **(A)**. Dashed lines highlight the start and end points of the experiment. **(B)** Tumor burden (tumor to body weight ratio) as % in LD (n = 9) or CRD (n = 10) conditions. Column data represent the mean ± SEM values for individual animals. The effect of CRD on tumor initiation is shown in **(C)**. Number of metastatic foci in the lungs of LD (n=6) and CRD (n =7) mice at the time of their sacrifice is shown in **(D)**. P-value obtained from a binomial two-sided test. Indicated (n) represents the number of independent experiments as biological replicates. Metastatic foci in the lungs are shown using H&E staining, scale bar 150 µm **(E)**. CRD-induced lung metastasis in 4T1 tumor model in BALB/cJ mice as shown by the graphical representation **(F)** and H&E staining **(G),** scale bar 100 µm. **(H)** The percentage of CD49f-breast cancer stem cell (CSC) subpopulations in LD and CRD tumors is shown as a graph. Results represent the mean ± SEM of 3–4 independent experiments. P-value obtained from an unpaired two-sided *t*-test. Mammosphere formation efficiency (MFE%) of LD and CRD tumor cells (n =3) is shown in Figure. **(I)** with lines indicating the mean ± SEM. P-value obtained from an unpaired two-sided *t*-test. The formation of organoids (tumoroids) from LD and CRD tumors is shown in the **J**. Scale bar, 250 µm.

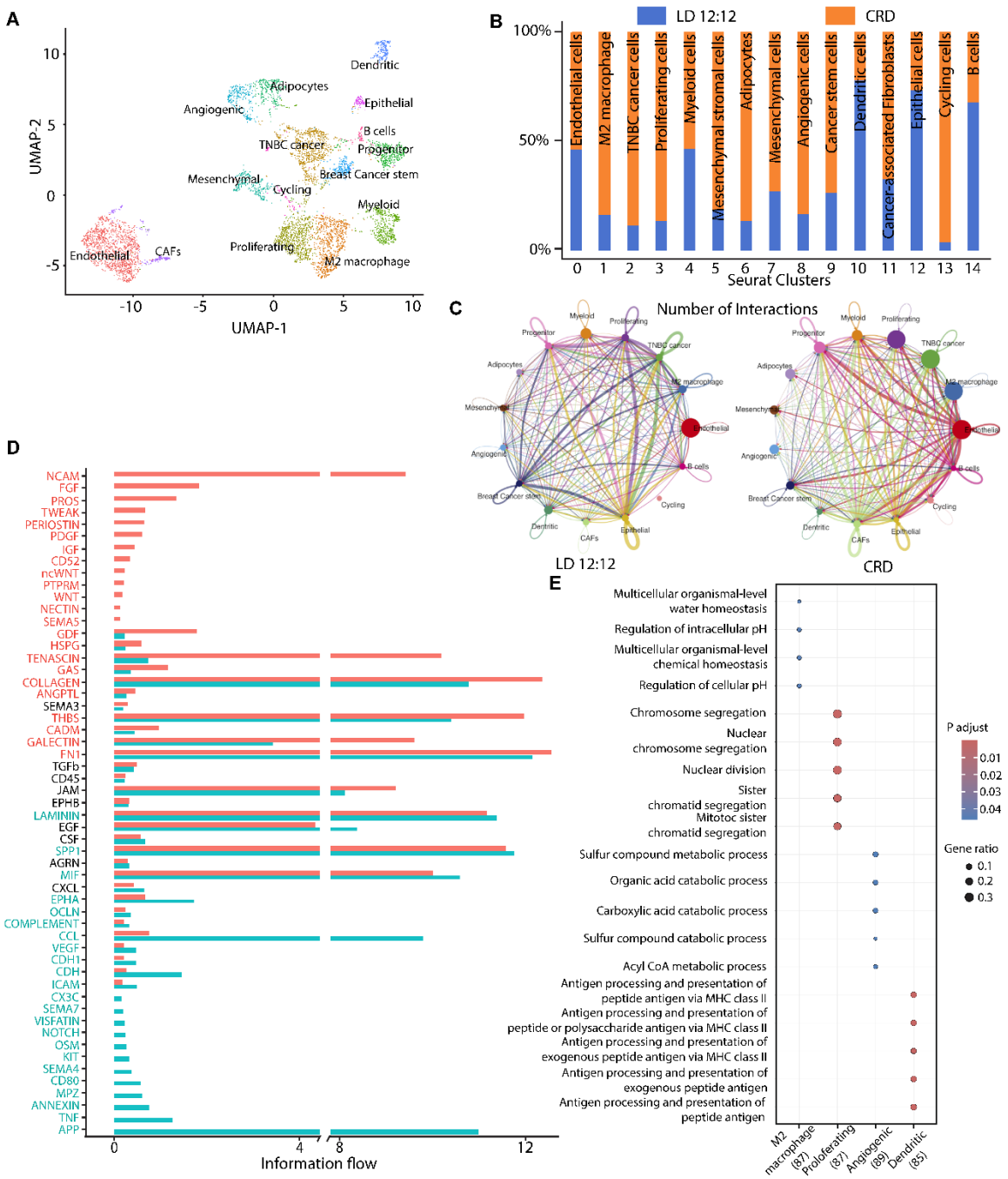

Fig. 3. CRD alters the tumor microenvironment. Cell clusters from 10x Genomics scRNA-seq analysis visualized using Uniform Manifold Approximation (UMAP). Colors indicate clusters of various cell types **(A)**. Fraction of cells from tumors (LD and CRD) in each cluster **(B)**. Clusters were annotated for their cell types as predicted using canonical markers and signature-based annotation with Garnett. Expression markers for endothelial cells (*KLF2*), M2 macrophages (*SLC2A1*), TNBC cancer cells (*TRPS1*), proliferating cells (*TOP2A)*, myeloid cells (*FTH1)*, progenitor cells (*NES*), adipocytes (*CLEC11A*), mesenchymal cells (*S100A4*), angiogenic cells (*RPL35A*), breast cancer stem cells *(FXYD3*), dendritic cells (*CD68*), cancer-associated fibroblast (*COL1A2*), epithelial cells (*EPCAM*), cycling cells (*CDK4*), and B-cells (*CD83*). The comparison of the total number of interactions among different cell populations between LD and CRD tumors

985 is shown in **C**. Edge width is proportional to the number of interactions, which assesses the number
986 of ligand–receptor pairs contributing to the communication between two interacting cell
987 populations. CellChat analysis quantitatively analyzes intercellular communication networks **(D)**.
988 The analysis shows differential ligand–receptor interactions between LD and CRD tumors.
989 Significant signaling pathways were ranked based on differences in the information flow within
990 the inferred networks between LD and CRD tumors. Dot plot profiling of the Gene Ontology (GO)
991 analyses in each cluster **(E)**. The dot plot represents the average expression of GOs per cluster. The
992 color gradient of dots represents the expression level, whereas the size represents the percentage
993 of cells expressing any genes per cluster. The number indicates the total number of genes identified
994 belonging to GO pathways significantly enriched in the cluster.
995

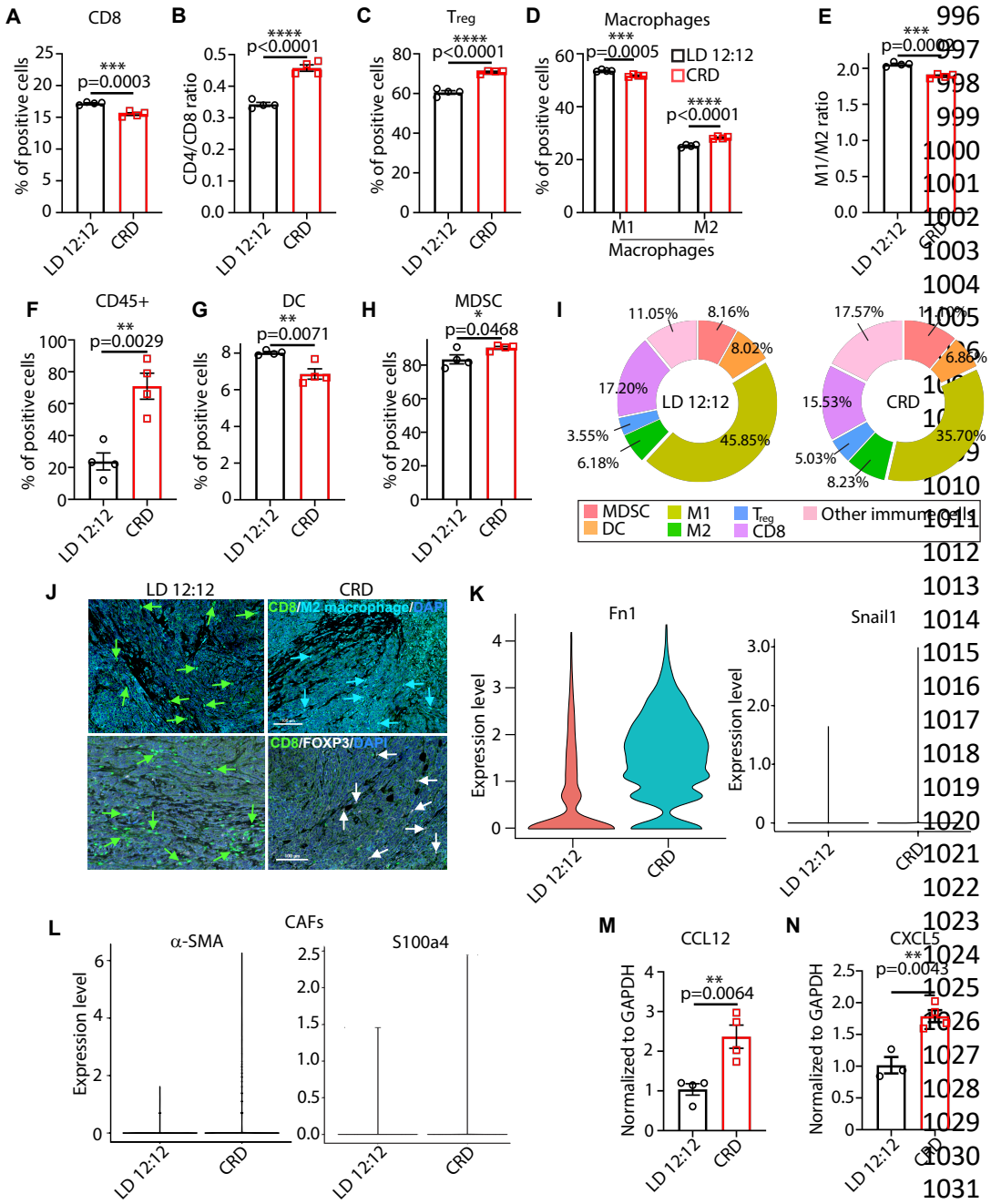

Fig. 4. CRD turns tumors "cold." Flow cytometry showed a significant decrease in cytotoxic CD8 T cell population (A). An overall ratio of CD4/CD8 is shown in **(B)**. Flow cytometry revealed a significant increase in the FoxP3^{+} T_{reg} population in the tumors of CRD mice (n = 4) **(C).** The percentage of antitumor M1 macrophage population and pro-tumor M2 macrophage population (n = 4) in LD and CRD-induced 4T1 tumors is shown in **(D),** and an overall ratio of M1/M2 is shown in **(E)**. The percentage of total leukocytes (CD45^{+} cells) in LD and CRD-induced tumors is shown in **(F)**. The percentage of DC cells **(G)** and MDSC **(H)** is shown in LD and CRD-induced tumors via flow cytometry (n=4). P-value obtained from an unpaired two-sided *t*-test. The relative distribution of key immune cell types in LD and CRD-induced tumors is represented in the donut chart **(I).** Representative immunostaining image of cytotoxic CD8 T-cell (CD8, green), M2

1042 macrophages (CD186, Cyan), and T_{reg} (FOXP3, White) in the LD and CRD-induced GEMM
1043 tumors (n = 4) Scale bar= 100µm **(J)**. Single-cell RNA seq (scRNA Seq) study showed epithelial
1044 to mesenchymal (EMT) markers (Fibronectin and Snail1) **(K),** and cancer-associated fibroblast
1045 (CAF) population based on S100a4, and α-SMA markers **(L),** in LD and CRD-induced tumors.
1046 The expression of chemokines *Ccl12* **(M)** and *Cxcl5* **(N),** is shown using real-time PCR in LD and
1047 CRD-induced tumors (n = 3 - 4).
1048

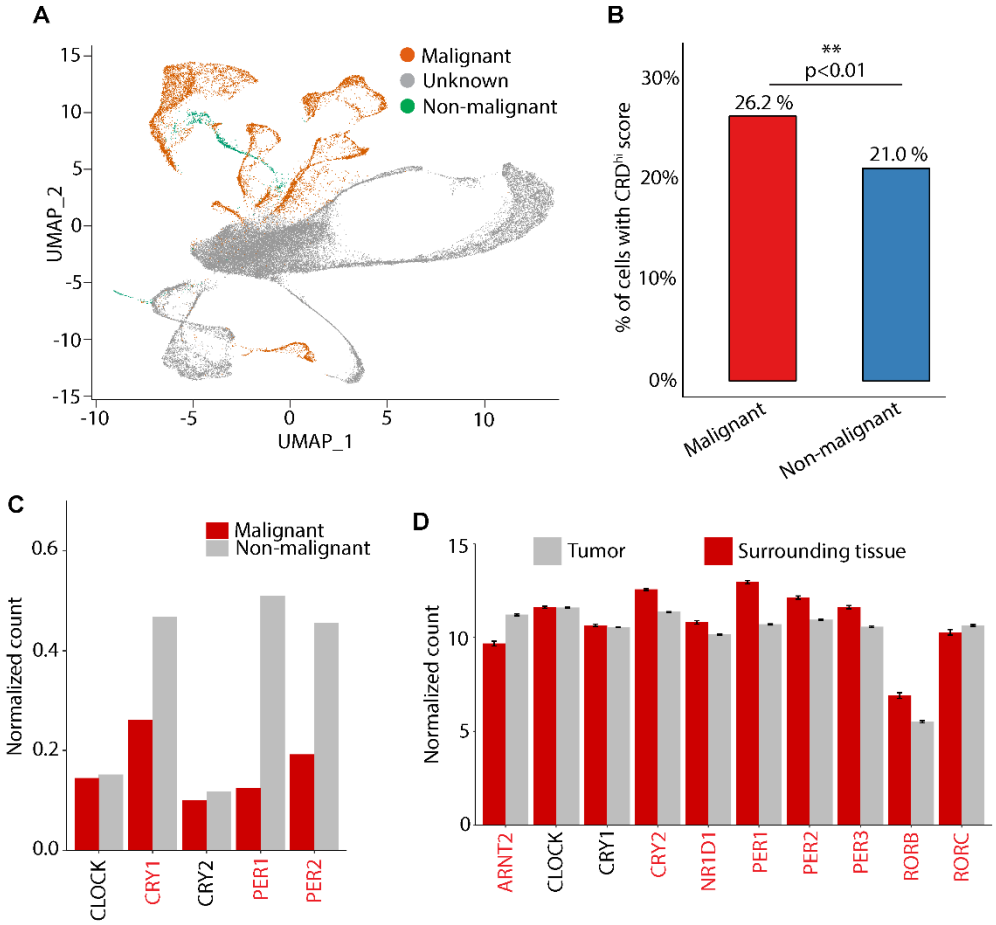

Fig. 5. The human circadian clock is disrupted in breast cancer. UMAP of malignant and nonmalignant cells (total cells = 42,512) captured across patients with (n = 9) triple-negative breast tumors. Moving from the plot in **A**, 30,719 cells had an unknown inferCNV call and 11,793 had a known inferCNV call. These 11,793 single cells were used for downstream analysis to detect "malignant" and "nonmalignant" cells. The percentage of malignant and nonmalignant cells with CRD^{high} is shown in **B**. The mean normalized expression values of the core circadian genes by the cell type (malignant and nonmalignant) are presented in **C**. Red represents significant changes in expression between malignant and nonmalignant cells. **(D)** The mean expression of the clock genes (+/- standard error of mean) over patients by the type of tissue analyzed in TNBC tumors (n = 1104) and surrounding tissue (n = 113) using TCGA.

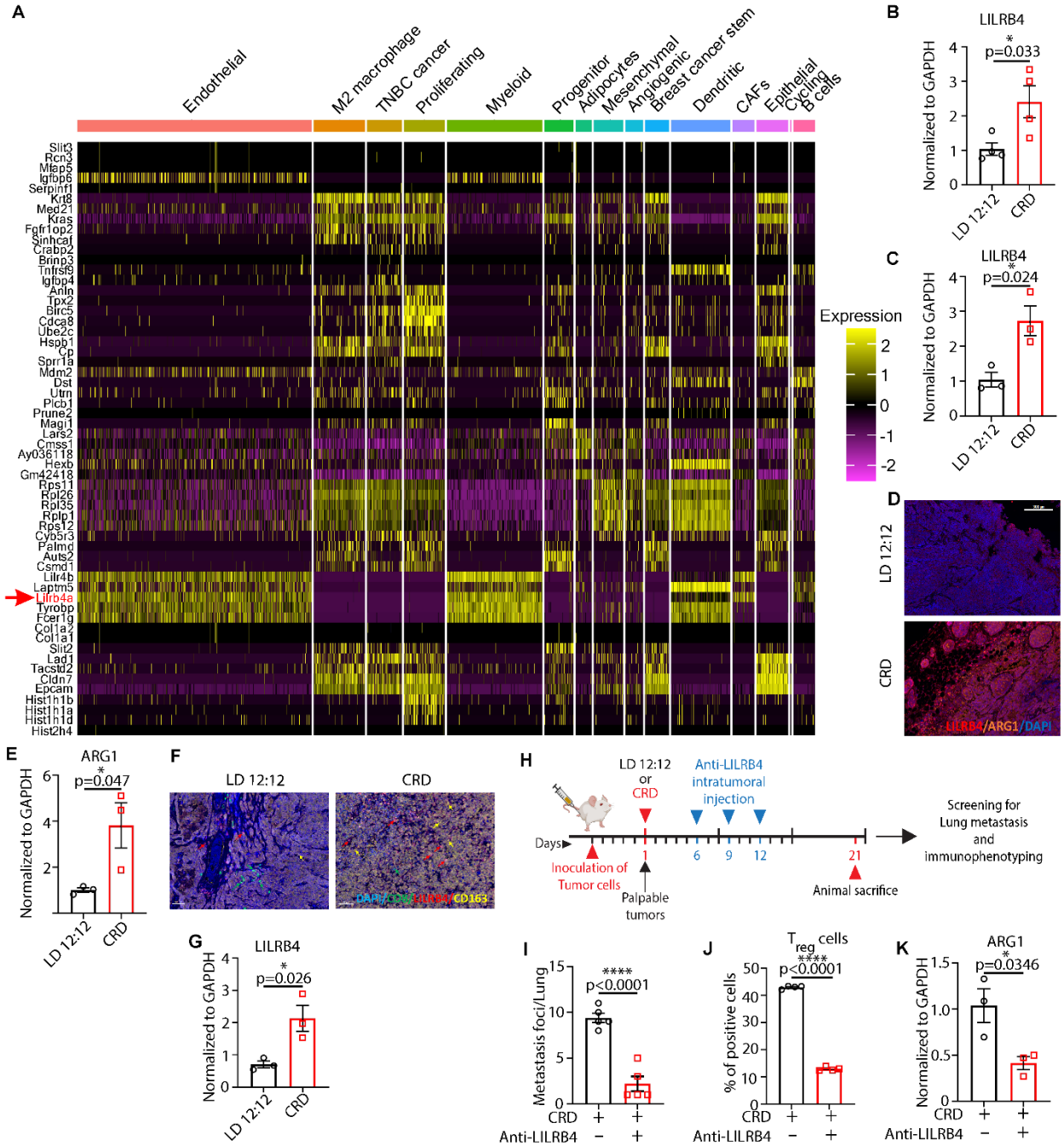

Fig. 6. CRD enhances LILRB4a expression to create an immunosuppressive tumor microenvironment. (A) Heatmaps of differentially expressed genes between LD 12:12 and CRD tumors identified using DESeq2 analyses of scRNA-seq. The transcript level of LILRB4 was analyzed in LD and CRD-induced GEMM tumors **(B)** and 4T1 tumors **(C)** using real-time PCR. **(D)** The expression of arginase 1 (*Arg1*, a downstream target of LILRB4a) was analyzed using immunofluorescence. Scale bar: 300µm **(E)** The transcript level of *Arg1* in LD and CRD-induced GEMM tumors was analyzed using real-time PCR. **(F)** Representative MxIF showing the expression of LILRB4, CD8, CD163, and FOXP3 markers in LD and CRD-induced GEMM tumors. Scale bar: 50µm. **(G)** The transcript level of *Lilrb4* in LD and CRD-induced mammary glands was analyzed using real-time PCR. **(H)** 4T1 cells were injected into the mammary fat pads

of BALB/cJ mice for the LILRB4-targeted immunotherapy. The number of metastatic foci in the lungs of CRD (control) and CRD (LILRB4-antibody) mice at the time of their sacrifice is shown in **I.** The percentage of T_{reg} cells in control and LILRB4-antibody-treated CRD-induced tumors is shown in **J.** The transcript level of *Arg1* in control and LILRB4-antibody-treated CRD-induced tumors is shown by real-time PCR **(K).**

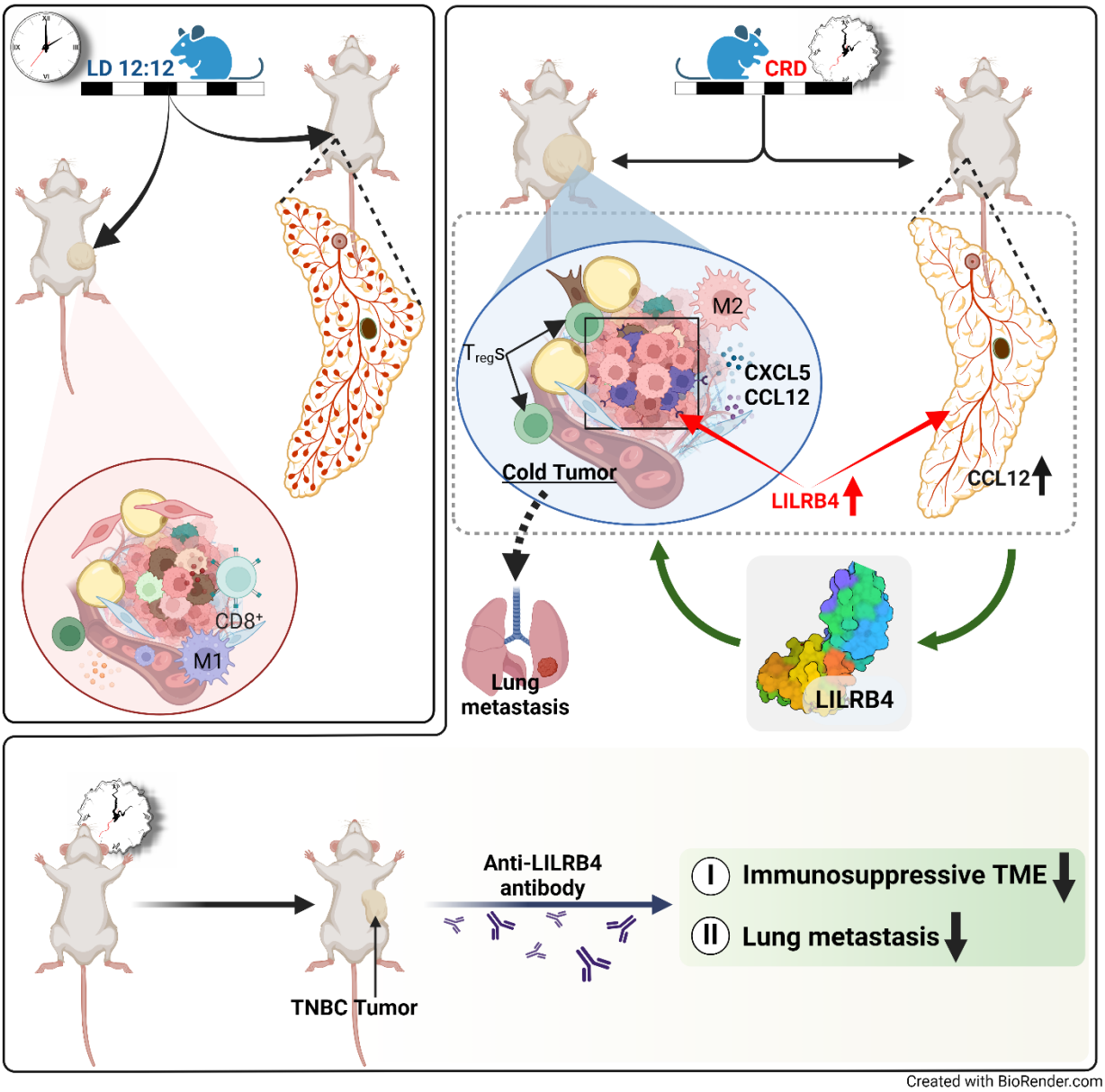

Fig 7. Diagrammatic representation of the molecular mechanism of CRD-induced immunosuppressive microenvironment in breast cancer. CRD enhances aggressive TNBC and lung metastasis by creating an immunosuppressive tumor microenvironment. CRD also disrupts the mammary gland morphology. Our study revealed that CRD enhanced LILRB4 expression, which induces an immunosuppressive "cold" TME by increasing the M2 macrophage and T_{reg} populations and decreasing M1 macrophage infiltration. Inhibition of LILRB4 via LILRB4-targeted antibody alleviates CRD-induced immunosuppressive TME and inhibits lung metastasis.